Sensors and Materials, Vol. 33, No. 7 (2021) 2385–2395
MYU Tokyo

S & M 2624

Cyclonic Motion and Structure in Rotating Tank: Experiment and Theoretical Analysis

Hung-Cheng Chen,[1] Jai-Houng Leu,[1*] Yu-Liang Lin,[2] Hong-Peng Liu,[3] Chong-Lin Huang,[4] Ho-Sheng Chen,[4] and Tian-Syung Lan[4]

[1]School of Intelligent Manufacturing, Shandong Polytechnic, No. 23000, Jin Ten East Road, Jinan City, Shandong Province, 250104, China
[2]School of Urban Rail, Shandong Polytechnic, No. 23000, Jin Ten East Road, Jinan City, Shandong Province, 250104, China
[3]School of Railway, Shandong Polytechnic, No. 23000, Jin Ten East Road, Jinan City, Shandong Province, 250104, China
[4]College of Mechatronic Engineering, Guangdong University of Petrochemical Technology, Maoming Guangdong, 525000, China

(Received January 4, 2021; accepted April 15, 2021)

Keywords: rotating tank, strong vortices, surface depression measurement, potential vorticity conservation

Theoretical analysis and a laboratory experiment were carried out to validate a gradient wind balance (GWB) vortex model by simulating hurricane-like cyclonic motion in a rotating tank with a gently sloping bottom. The analysis clarified the effects of the motion on the conservation of potential vorticity of shallow water. The effects include the topography of the sloping bottom, vortex depression, and parabolic-free-surface deformation. The velocity distribution of the vortex was identified by measuring the vortex depression with a vertical laser light sheet and fitting it with the GWB model. The result provides a clear view of the entire vortex structure to understand vortices with large Rossby numbers in geophysical flows.

1. Introduction

Simulations of coherent geophysical vortices that travel a long distance have attracted extensive attention during the past decades and demonstrated the strong similarity of flow patterns between experimental and real vortices.[1–11] Depending on the order of magnitude of the Rossby number of cyclonic motion, the embedded dynamics reveal different pictures of the flow in the self-propagation β-drift,[1–3] Rossby wave generation,[4] and vortex/topography interaction.[5,6] Most previous studies focused on vortices with low Rossby numbers [$Ro \approx O(10^{-2}) - O(10^{-1})$].[1–4] In contrast, our interest mainly lies in hurricane-like cyclonic motion with high Rossby numbers [$Ro \approx O(1) - O(10)$].[12–15] Several studies investigated cyclonic motion in a rotating tank with a sloping bottom topography. Firing and Beardsley conducted the first laboratory experiment on an isolated barotropic eddy on a β-plane.[2] By generating the eddy on a bottom with a gentle slope ($s_y \approx 0.1$) in a sliced-cylinder geometry, it was found that

*Corresponding author: e-mail: jahonleu@yahoo.com.tw
https://doi.org/10.18494/SAM.2021.3290

ISSN 0914-4935

the eddy rapidly evolved to establish a dipole. They attempted to validate the initial northwestward translation of the vortex on the β-plane as well as the sliced-cylinder analogy to the large-scale wind-driven problem as predicted earlier by Adem.[1]

A sloping bottom in a rotating tank is important in reproducing the effect of the planetary vorticity gradient in the meridional direction, the β-effect. To simulate such ideal cyclonic motion in a rotating tank, the two-dimensional quasi-geostrophic vorticity equation (QGVE) has generally been employed to investigate the specific flow field for a vortex with a low Rossby number. Masuda *et al.*[4] conducted a laboratory and numerical study of an isolated eddy in a rectangular tank with a steep bottom slope of s_y~0.33. They confirmed that the vortex evolved into a larger main eddy and several secondary eddies, showing the significant influence of the strong β-effect on the cyclonic vortex. For a long-lived vortex translating on a gently sloping bottom of s_y~0.133, Carnevale *et al.*[5] generated monopolar vortices using stirred/sink methods and simulated the motion by numerically solving a QGVE.

However, there have been few investigations of the significance of dimensionless parameters by the conservation of potential vorticity (PV) for cyclonic motion in a rotating tank. Thus, here we focus on investigating vortex structures with a large Rossby number and simulate hurricane-like strong cyclonic motion in a rotating tank with a gently sloping bottom to propose dimensionless parameters. As the gradient wind balance (GWB) vortex model captures the features of strong vortices better than other models and accurately identifies the structure of vortices, a theoretical analysis of the GWB vortex model provides a better understanding of the motion of tropical cyclones than that obtained from previous research. The Gauss–Newton method of nonlinear regression is used to fit the GWB vortex model with high accuracy, enabling the identification of the vortex structure by using the size and shape parameters of the vortex depression. The model shows the significance of the vortex β-effect that occurs in the motion of hurricane-like vortices in nature by visualization using a vertical laser light sheet. The velocity distribution of the vortex is calculated using the fitted GWB vortex model and is verified by the visualization of a horizontal laser light sheet. The visualization requires an octahedral high-speed rotating prism with a post-objective scanning technique and a high-resolution CCD camera to produce and sense the trajectories of tracer particles in a thin and bright laser light sheet. By choosing the appropriate exposure time of cyclonic motion for a preset frame speed, information on the vortex structure is obtained. Image sensor technologies enable the capture of images of the cyclonic motion in well-controlled exposure times. The results of this study contribute to providing an insight into identifying the vortex structure using the GWB vortex model and three-dimensional streak photography with advanced sensor technology.

The paper is organized as follows. Section 2 presents the physical parameters of the rectangular rotating tank and describes the conservation of PV, which is incorporated into a GWB vortex model as the initial condition. Section 3 explains the experimental procedures of the tank experiment, vortex generation, and flow visualization. Section 4 presents the trajectories of cyclonic vortices over time. Finally, conclusions are presented in Sect. 5.

2. Governing Equations

2.1 Geometric parameters

Maximum deformation of the parabolic free surface (d)

Figure 1(a) shows the top view of the rectangular water tank. The horizontal dimensions of the tank are $L \times M$ and the origin of the local Cartesian coordinates (0, 0) coincides with the geometric center of the tank. Figure 1(b) shows the flow condition of the rectangular water tank before it starts to rotate, where H_0 represents the initial fluid depth and s_y is the slope of the bottom plate. The x, y, and z directions in local Cartesian coordinates are horizontally eastward, horizontally northward, and vertically upward, respectively. Figure 1(c) shows the flow configuration of the tank when it rotates at a constant speed of $\Omega = f / 2$, where f is the Coriolis parameter of the rotating tank. Paraboloidal surface deformation due to the rotation of the tank occurs in the absence of fluid motion. We simulate this deformation of the free surface as the bottom paraboloidal topography h_p. Thus, a so-called modified unperturbed layer depth H_m is introduced. The paraboloidal topography h_p can be expressed as $h_p = d - \Omega^2 r^2/2g$, where d is the maximum deformation of the parabolic free surface and proportional to the radial distance from the tank center r, the rotation speed Ω, and the dimensions L and M [Fig. 1(c)].

d is calculated at the corner of the tank as

$$d = \max \frac{\Omega^2 r^2}{2g} = \frac{\Omega^2 \left(L^2 + M^2 \right)}{8g}. \tag{1}$$

Minimum height of parabolic free surface (D) and modified unperturbed layer depth (H_m)

As shown in Fig. 1(c), the modified unperturbed layer depth H_m can be expressed as $H_m \equiv D + d$, where D is the minimum height of the parabolic free surface at the geometric center

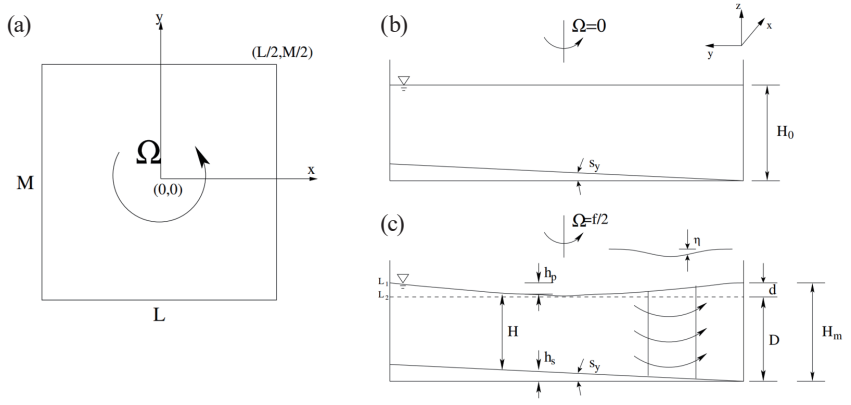

Fig. 1. Schematic of cyclonic vortex motion in a constant-speed, rotating tank with a sloping bottom. (a) Top view of the tank, whose center is located at the origin. (b) Side view of the tank before it starts to rotate. (c) Side view of the rotating tank.

of the tank. D is calculated by considering the mass conservation of the tank fluid before and after the rotation. The volume of the fluid between height levels L_1 and L_2 before and after the rotation of the tank must be the same. That is,

$$(H_0 - D)LM = \int_{-M/2}^{M/2}\int_{-L/2}^{L/2}(d - h_p)dxdy. \tag{2}$$

Substituting Eq. (1) in Eq. (2) yields

$$(H_0 - D)LM = \int_{-M/2}^{M/2}\int_{-L/2}^{L/2}\frac{\Omega^2 r^2}{2g}dxdy = \frac{\Omega^2 LM(L^2 + M^2)}{24g}, \tag{3}$$

where $r^2 = x^2 + y^2$. Finally, D is obtained from Eq. (3) as $D = H_0 - \Omega^2(L^2 + M^2)/24g$. The modified unperturbed layer depth H_m is thus obtained as

$$H_m \equiv H_0 + \frac{\Omega^2(L^2 + M^2)}{12g}. \tag{4}$$

2.2 Conservation of PV

The governing principle for the rotation of a shallow fluid is the law of conservation of PV:[16,17]

$$\frac{D\Pi}{Dt} = 0, \tag{5}$$

where PV is defined as $\Pi = (f + \zeta)/H$ with f the planetary (background) vorticity, ζ the relative vorticity, and H the fluid layer depth. We consider a rotating fluid in a tank with a bottom having a gentle slope s_y, where the tank rotates at a constant speed of $\Omega = f/2$ with f the Coriolis parameter of the rotating fluid. Then, we let $h_B(x, y) = h_s + h_p$ be the topographic features, where the sloping bottom topography h_s is expressed as $h_s = s_y y'$ with the meridional coordinate $y' = y + M/2$ used for convenience. The behavior of the fluid in the tank experiment is described by the law of conservation of PV by assuming small variations of η and $h_B = s_y y' + h_p$ with respect to H_m, i.e., $\eta / H_m << 1$, $s_y y' / H_m << 1$, and $h_p / H_m << 1$. Equation (5) can thus be written as

$$\frac{D}{D_t}\left(\frac{1}{H_m}\left(f\left(1 - \frac{\eta}{H_m} + \frac{s_y y'}{H_m} + \frac{h_p}{H_m}\right) + \varsigma\left(1 - \frac{\eta}{H_m} + \frac{s_y y'}{H_m} + \frac{h_p}{H_m}\right)\right)\right) = 0 \tag{6}$$

Next, we scale the cyclonic vortex motion. With the maximum tangential speed of the vortex V_m as a reference, the corresponding radius R_m is regarded as the reference length, $\varsigma_m = V_m / R_m$ as the reference vorticity, and ς_m^{-1} as the reference time (the vortex turn-around time). We choose the maximum vortex depression η_v (as shown in Fig. 1) as the reference free-surface depression, and thus a set of non-dimensional variables are defined by $t^* = tV_m / R_m$, $y^* = y / R_m$, $\eta^* = \eta / R_m$, $h_p{}^* = h_p / H_m$, and $\varsigma^* = \varsigma / \varsigma_m$.

Since f / H_m is constant, we divide Eq. (6) by $\varsigma_m{}^2 / H_m$ to obtain

$$\frac{D}{Dt^*}\left(\beta_y^* y'^* - \beta_v^* \eta^* + \beta_p^* h_p^* + \varsigma^* \left(1 + s_y^* y'^* - s_v^* \eta^* + s_p^* h_p^*\right)\right) = 0. \tag{7}$$

Equation (7) describes the non-dimensional PV conservation relationship for cyclonic motion in a rotating tank. In Eq. (7), there are six non-dimensional parameters: (i) the bottom slope parameter $s_y{}^* = s_y R_m / H_m$, where s_y represents the bottom slope, (ii) the bottom β-parameter $\beta_y{}^* = f s_y R_m{}^2 / V_m H_m = s_y{}^* / Ro_v$, where Ro_v is the vortex Rossby number defined as $Ro_v = V_m / f R_m$, (iii) the vortex slope parameter $s_v{}^* = \eta_v / H_m = s_v R_m / H_m$, where the characteristic vortex slope s_v is defined as $s_v = \eta_v / R_m$, (iv) the vortex β-parameter $\beta_v{}^* = f s_v R_m{}^2 / V_m H_m = s_v{}^* / Ro_v$, (v) the free surface slope parameter $s_p{}^* = h_p / H_m = s_p R_m / H_m$, where the characteristic free surface slope s_p is defined as $s_p = h_p / R_m$, and (vi) the free surface β-parameter $\beta_p{}^* = f s_p R_m{}^2 / V_m H_m = s_p{}^* / Ro_v$.

2.3 GWB vortex model

To simulate strong cyclonic vortices [Fig. 1(c)], the following axisymmetric, two-parameter GWB vortex model was used to fit the initial vortex distribution:[10]

$$H\left(x, y, t = 0\right) = H_m - \eta_v \left(1 - \exp\left(-A\tilde{r}^{-B}\right)\right) - h_B, \tag{8}$$

$$v_\theta\left(x, y, t = 0\right) = -\frac{f\tilde{r}}{2} + \sqrt{\frac{f^2\tilde{r}^2}{4} + gAB\eta_v \exp\left(-A\tilde{r}^{-B}\right) / \tilde{r}^B}, \tag{9}$$

where v_θ is the azimuthal velocity of the vortex, g is the gravitational acceleration, $\tilde{r}$ is the radial distance of each fluid particle from the vortex center, A is the vortex size, and B is the shape parameter.

3. Experiments

The experiments were conducted in a rectangular water tank made of glass with dimensions of 135 × 135 × 40 cm^3. Figure 2(a) illustrates the experimental setup. By varying the rotation

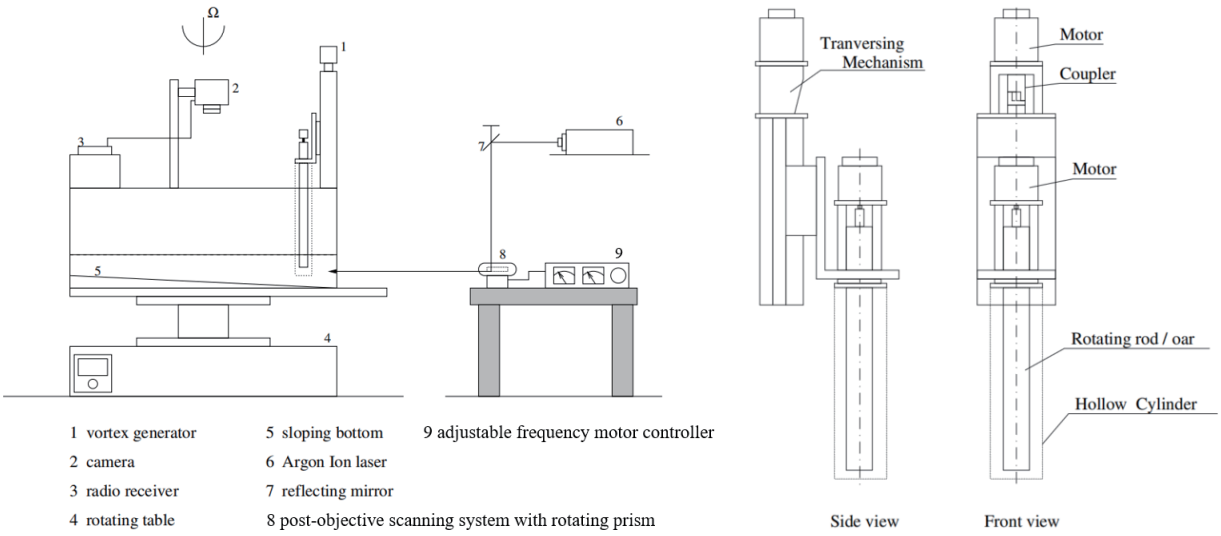

Fig. 2. (a) Schematic of the experimental setup and (b) schematic of stir-induced vortex generator.

speed of the table between 0.3 and 10 RPM, the free surface of the fluid was adjusted centrifugally to a parabolic shape when the fluid reached the state of solid-body rotation. After reaching the state of solid-body rotation in about 30 min, a cyclonic vortex was generated by a cylinder and an oar with diameters of 4 and 5 cm, respectively, in a thin-walled hollow cylinder with a diameter of 10 or 15 cm, which rotated concentrically in parallel with the axis of the rotating table at an angular speed of 20.8 rad/s [Fig. 2(b)]. An outer hollow cylinder was used to confine the disturbance of the fluid caused by the rotation of the inner cylinder. In the experiment, a gently sloping bottom of around 3° was placed in the rotating tank to simulate the planetary β-effect.

The flow field was visualized by horizontal streak photography. The surface depression in a local vortex was measured by using a vertical laser light sheet. Streak photography of tracer particles was performed by adding spherical polyamide particles to the fluid while the plane of interest was illuminated by a laser sheet. The laser light sheet was made by a laser beam from a 4 W argon-ion laser. The laser light beam was then enhanced and reflected by an octahedral prism (Lincoln Laser Company) rotating at a high speed (typically around 6000 rpm) onto a thin light sheet with a fan region of 90°. The rotating prism with post-objective scanning provided a wide and bright observation area. This technique places the focal plane on the octahedral prism, and the imaging lens is a relatively simple component located in front of the prism.[18]

To visualize the depression of the vortex, a vertical light sheet was made by a diode laser with an output of about 130 mW, which was mounted on the tank. Appropriate positioning of the light sheet on the vortex allowed slice-by-slice recording of the surface profiles as the vortex passed. The vortex depression was obtained by subtracting a reference frame from the corresponding profile. The spatial resolution of the surface profile measurement was 0.01 mm.

4. Results and Discussion

The initial conditions of the experimental vortices were identified using the GWB vortex model. The associated distributions of the azimuthal velocity were fitted by the model through non-intrusive measurement of the surface depression of the vortex. The time evolution and the structure of the vortex were captured by streak photography under illumination by a laser light sheet. The experiments were conducted in a rotating tank with a low angular speed of $\Omega = 0.785$ rad/s, a tank bottom slope s_y of 0.0538 rad, a water depth in the tank H_0 of around 13 cm, and a modified unperturbed layer depth H_m of 14.91 cm calculated using Eq. (4).

4.1 Initial vortex structure

To clarify the effect of the vortex depression on cyclonic motion, we generated vortices with a Rossby number of $O(1)$, corresponding to significant surface depression. Two typical vortices *S* and *W* with different strengths were generated. A depression was generated in *S* using a rotating oar, which was larger than the depression in *W* generated using a rotating solid cylinder. The initial condition was determined as that when the vortices became visually clean and stable, which took 5 and 6 s for *S* and *W*, respectively.

Figures 3(a) and 3(b) illustrate the surface profiles of vortex *S* at a position approximately 52 cm from the southern end of the tank. Figure 3(a) shows the reference photograph taken from the northern end of the tank before the vortex arrived at the illuminating vertical plane, while the photograph in Fig. 3(b) was taken when the vortex center was passing through the light sheet. The actual surface depression of the vortex was then obtained by subtracting the two profiles presented in Figs. 3(a) and 3(b). The fitted profile of the vortex depression was obtained by nonlinear regression using the Gauss–Newton method and exhibited good agreement with the experimental result.

Figures 4(a) and 4(b) respectively display the fitted results of the vortex depression and the azimuthal velocity distributions of *S* and *W*. The vortex size and shape parameters *A* and *B* in

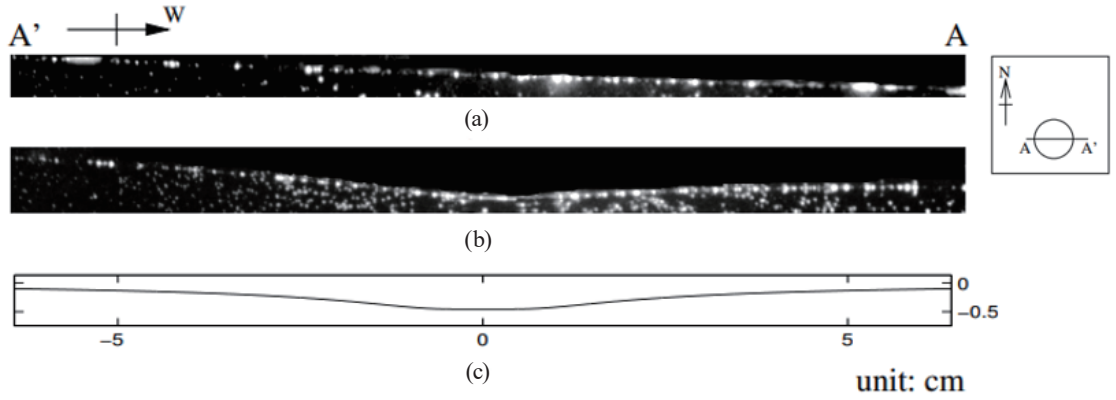

Fig. 3. Photographs showing the surface profiles of a cyclonic vortex illuminated by a vertical laser light sheet. (a) Reference profile, (b) profile at the vortex center, and (c) fitted profile.

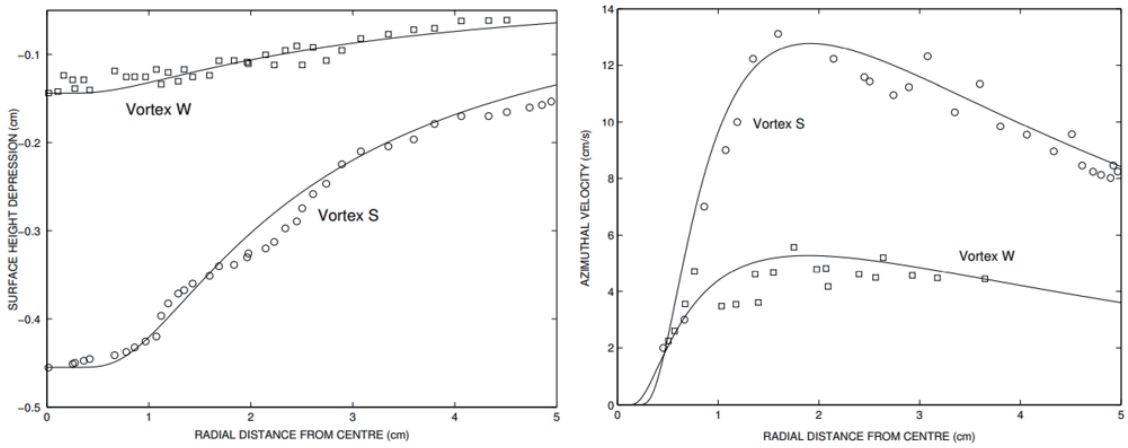

(a) (b)

Fig. 4. Structures of the cyclonic vortices represented by (a) surface depression and (b) velocity distribution in the radial direction. Circles represent the measured values of vortex *S* and squares denote the measured values of vortex *W*. Solid lines represent the values obtained using the GWB vortex model.

Eqs. (8) and (9) are 2.585 and 2.482 for *S* and 1.242 and 0.893 for *W*, respectively. This result shows the similarity between the measured values and the azimuthal velocity of the two vortices obtained with the GWB vortex model. Note that the azimuthal velocity obtained with the GWB vortex model is calculated using vortex parameters A, B, and η_v fitted using the vortex depression in Eq. (8). The azimuthal velocity is measured from digital images using particle tracking technology.[19] This method is based on Voronoi imaging and provides an accurate estimation of the two-dimensional velocity distribution. These images are captured by a high-resolution CCD camera. The results show some asymmetry of the measured azimuthal velocity due to the planetary β-effect.

4.2 Time evolutions and structures of cyclonic vortices

Figure 5 illustrates the results of streak photography of tracer particles for the free motion of *S* on a sloping bottom in a rotating tank in an area of 12 × 12 cm^2. The vortex was generated about 45 and 40 cm away from the south and east boundaries, respectively, to avoid the boundary effect. After a monopolar vortex was generated, it moved to the northwest due to the β-effect from the sloping bottom of the water tank. Similar results were observed for *W* in an area of 17 × 17 cm^2 (Fig. 6). According to the streakline patterns in the lower-right part of Figs. 5(b)−5(f), a weak anticyclonic vorticity region existed in the outside of the monopolar vortex structure. This feature was induced by the Rossby wave effect of the vortex and was more prominent in *S* than in *W*. These two vortices moved northwestward.

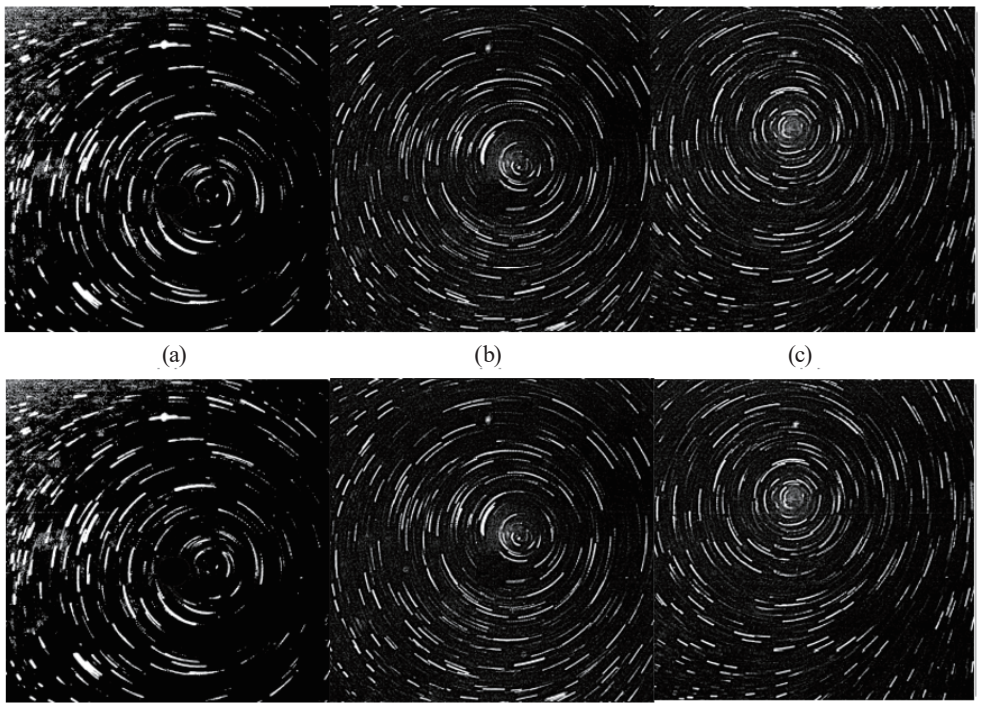

Fig. 5. Plane-view photographs showing the evolution of vortex *S* at times of (a) 5, (b) 9, (c) 11, (d) 13, (e) 15, and (f) 17 s after the vortex was generated.

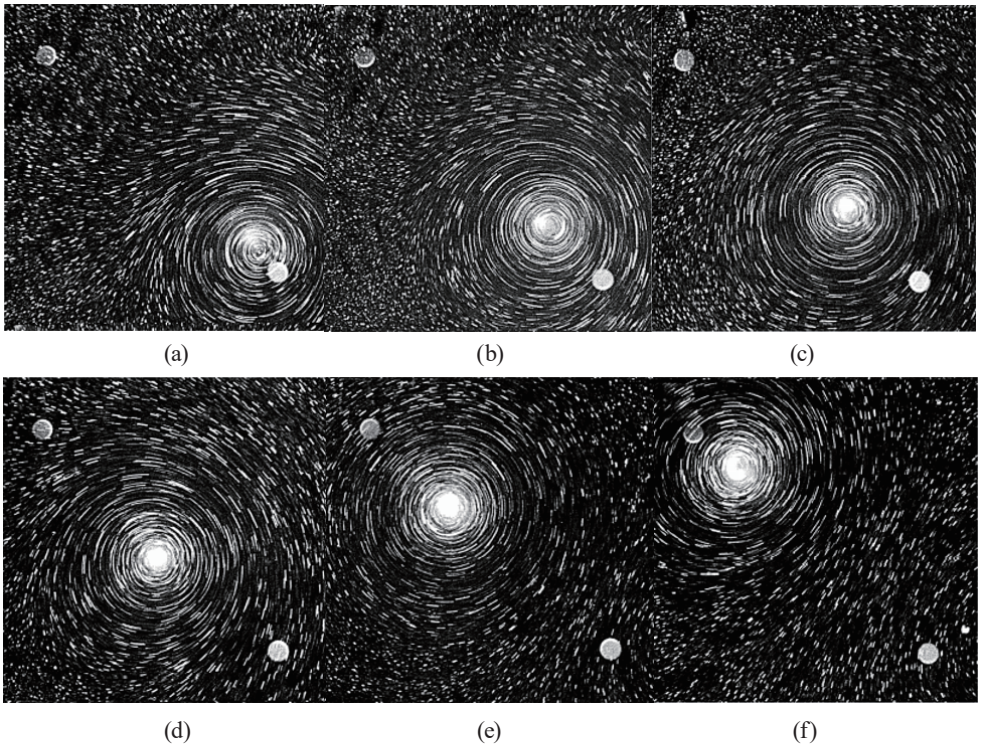

Fig. 6. Similar to Fig. 5 but for vortex *W* at times of (a) 6, (b) 10, (c) 14, (d) 18, (e) 22, and (f) 28 s after the vortex was generated.

Table 1
Summary of non-dimensional parameters of initial conditions of vortices *S* and *W*.

	V_m (cm/s)	R_m (cm)	η_v (cm)	Ro_v	s_y^*	s_v^*	s_p^*	β_y^*	β_v^*	β_p^*
Vortex *S*	12.9	1.9	0.455	4.32	0.0069	0.0305	0.0013	0.0016	0.0071	0.0003
Vortex *W*	5.3	1.9	0.144	1.78	0.0069	0.0097	0.0013	0.0039	0.0054	0.0007

4.3 Comparison of non-dimensional parameters with different strengths of vortex

To summarize the dynamical features of *S* and *W*, the calculated non-dimensional parameters that were derived in Sect. 2 are shown in Table 1. Vortices *S* and *W* have Rossby numbers of $O(1)$. The contribution of the β-like effects to the vortex motion can be estimated from the strength of three non-dimensional parameters β_y^*, β_v^*, and β_p^*. Among the three β-parameters, the vortex β-parameter is the largest, followed by the bottom and free surface β-parameters. The vortex β-parameters of *S* and *W* were about 4.4 and 23.6 times larger and 1.4 and 7.7 times larger than the bottom and free surface β-parameters, respectively. This indicates that the motion of *S* was significantly affected by the strength of the vortex itself, especially the deep surface depression of the vortex. The vortex β-parameter of *W* was close to the bottom β-parameter.

5. Conclusions

A non-intrusive optical method was used to measure the surface depression of a vortex to accurately adapt the azimuthal velocity distribution. For vortices with a large Rossby number, the change in the water depth near the vortex center had a significant influence on the overall motion of the vortex. An octahedral high-speed rotating prism adjusted to produce a thin and bright laser light sheet and an appropriate exposure time for capturing cyclonic motion enabled us to obtain complete information of the vortex structure through the illuminated trajectories of tracer particles.

Six dimensionless parameters were found by using the conservation law of PV, which represents the balance of the β-effects by three different depth changes. Through the measurement and model calculation of these three effects, the influence on the motion of the vortex in the rotating tank was investigated. The experimental results showed that a strong vortex had a stronger β-effect caused by the surface depression in the center of the vortex than the bottom and free surface β-effects. A weaker vortex had a vortex β-effect that was comparable to the bottom β-effect and stronger than the free surface β-effect. The initial structure of the vortex with a GWB can be used to identify the vortex structure by numerical calculation of the shallow water equation. The results of this study are expected to lead to a deeper understanding of hurricane-like vortex motion, for which further research is required.

Acknowledgments

The authors would like to thank Shandong Polytechnic, China, for their support of this research. The first author would also like to thank Professors C. C. Chu and C. C. Chang of National Taiwan University for their support in the early stage of this work.

References

1 J. Adem: Tellus **8** (1956) 364. https://doi.org/10.1111/j.2153-3490.1956.tb01234.x
2 E. Firing and R. C. Beardsley: J. Phys. Oceanogr. **6** (1976) 57. https://doi.org/10.1175/1520-0485(1976)006<0057:tboabe>2.0.co;2
3 M. Takematsu and T. Kita: Fluid Dyn. Res. **3** (1988) 400. https://doi.org/10.1016/0169-5983(88)90100-1
4 A. Masuda, K. Marubayashi, and M. Ishibashi: J. Fluid Mech. **213** (1990) 641. https://doi.org/10.1017/S0022112090002488
5 G.F. Carnevale, R. C. Kloosterziel, and G. J. F. van Heijst: J. Fluid Mech. **233** (1991) 119. https://doi.org/10.1017/s0022112091000411
6 E. J. Hopfinger and G. J. F. V. Heijst: Annu. Rev. Fluid Mech. **25** (1993) 241. https://doi.org/10.1146/annurev.fl.25.010193.001325
7 M. V. Nezlin and E. N. Snezhkin: Rossby Vortices, Spiral Structures, Solitons: Astrophysics and Plasma Physics in Shallow Water Experiments (Springer-Verlag, 1993). https://doi.org/3642881246
8 B. Cushman-Roisin and J.-M. Beckers: Introduction to Geophysical Fluid Dynamics: Physical and Numerical Aspects (Prentice-Hall, 2009) Chap. 1.
9 A. Stegner and V. Zeitlin: J. Fluid Mech. **356** (1998) 1. https://doi.org/10.1017/S0022112097008082
10 J. B. Flór and I. Eames: J. Fluid Mech. **456** (2002) 353. https://doi.org/10.1017/S0022112001007728
11 G. J. F. V. Heijst and H. J. H. Clercx: Annu. Rev. Fluid Mech. **41** (2008) 143. https://doi.org/10.1146/annurev.fluid.010908.165207
12 S. L. Huang, H. C. Chen, C. C. Chu, and C. C. Chang: Exps. Fluids **45** (2008) 267. https://doi.org/10.1007/s00348-008-0477-5
13 G. J. Holland: Mon. Wea. Rev. **108** (1980) 1212. https://doi.org/10.1175/1520-0493(1980)108<1212:aamotw>2.0.co;2
14 W. H. Schubert, M. T. Montgomery, K. T. Richard, T. A. Guinn, S. R. Fulton, J. P. Kossin, and J. P. Edward: J. Atmos. Sci. **56** (1999) 1197. https://doi.org/10.1175/1520-0469(1999)056<1197:PEAECA>2.0.CO;2
15 H. E. Willoughby, J. A. Clos, and M. G. Shoreibah: J. Atmos. Sci. **39** (1982) 395. https://doi.org/10.1175/1520-0469(1982)0392.0.CO;2
16 J. C. McWilliams: Fundamentals of Geophysical Fluid Dynamics (Cambridge University Press, 2011) Chap. 3.
17 J. Pedlosky: Geophysical Fluid Dynamics (Springer, 1986) Chap. 3.
18 G. F. Marshall and G. E. Stutz: Handbook of Optical and Laser Scanning (CRC Press, 2011) 2nd ed., pp. 269–272.
19 H. Capart, D. L. Young, and Y. Zech: Exps. Fluids **32** (2002) 121. http://doi.org/10.1007/s003480200013